

17 **Abstract**

18 Different entrainment-mixing processes can occur in clouds; however, a
19 homogeneous mixing mechanism is often implicitly assumed in most commonly used
20 microphysics schemes. Here, we first present a new entrainment-mixing
21 parameterization that uses the grid-mean relative humidity without requiring the
22 relative humidity of the entrained air. Then, the parameterization is implemented in a
23 microphysics scheme in a large eddy simulation model, and sensitivity experiments are
24 conducted to compare the new parameterization with the default homogeneous
25 entrainment-mixing parameterization. The results indicate that the new entrainment-
26 mixing parameterization has a larger impact on the number concentration, volume-
27 mean radius, and cloud optical depth in the stratocumulus case than in the cumulus case.
28 This is because inhomogeneous and homogeneous mixing mechanisms dominate in the
29 stratocumulus and cumulus cases, respectively, which is mainly due to the larger
30 turbulence dissipation rate in the cumulus case. Because stratocumulus clouds break up
31 during the dissipation stage to form cumulus clouds, the effects of this new entrainment-
32 mixing parameterization during the stratocumulus dissipation stage are between those
33 during the stratocumulus mature stage and the cumulus case. A large aerosol
34 concentration can enhance the effects of this new entrainment-mixing parameterization
35 by decreasing the cloud droplet size and evaporation time scale. The results of this new
36 entrainment-mixing parameterization with grid-mean relative humidity are validated by
37 use of a different entrainment-mixing parameterization that uses parameterized

38 entrained air properties. This study sheds new light on the improvement of entrainment-
39 mixing parameterizations in models.

40

41 **1. Introduction**

42 The process of entrainment and subsequent mixing between clouds and their
43 environment is one of the most uncertain processes in cloud physics, which is thought
44 to be crucial to many outstanding issues, including warm-rain initiation and subsequent
45 precipitation characteristics, cloud-climate feedback, and evaluating the indirect effects
46 of aerosol (Paluch and Baumgardner, 1989; Yum, 1998; Ackerman et al., 2004; Kim et
47 al., 2008; Huang et al., 2008; Del Genio and Wu, 2010; Lu et al., 2011; Lu et al., 2014;
48 Kumar et al., 2013; Zheng and Rosenfeld, 2015; Fan et al., 2016; Gao et al., 2020; Gao
49 et al., 2021; Zhu et al., 2021; Xu et al., 2021; Kumar et al., 2013; Yang et al., 2016;
50 Yang et al., 2021). The most well-studied concepts are homogeneous/inhomogeneous
51 entrainment-mixing mechanisms. During homogeneous mixing, all droplets experience
52 evaporation, and no droplet is evaporated completely. During extremely
53 inhomogeneous mixing, some droplets near the entrained air evaporate completely,
54 while the remaining droplets maintain their original sizes. If the situation is somewhere
55 between these two extreme scenarios, an inhomogeneous mixing process occurs. Some
56 studies suggest that homogeneous mixing is likely to be typical (Jensen et al., 1985;
57 Burnet and Brenguier, 2007; Lehmann et al., 2009), whereas others have claimed that
58 extremely inhomogeneous scenario is dominant (Pawlowska et al., 2000; Burnet and

59 Brenguier, 2007; Haman et al., 2007; Freud et al., 2008; Freud et al., 2011). Different
60 mechanisms can be undistinguishable when the relative humidity in the entrained air is
61 high (Gerber et al., 2008).

62 Some sensitivity studies assuming homogeneous or extremely inhomogeneous
63 mixing have found that different mixing mechanisms can significantly influence the
64 microphysics and radiative properties of clouds (Lasher-Trapp et al., 2005; Grabowski,
65 2006; Chosson et al., 2007; Slawinska et al., 2008). For example, Grabowski (2006)
66 used a cloud-resolving model and found that the amount of solar energy reaching the
67 surface in the pristine case, assuming the homogeneous mixing scenario, is the same as
68 in the polluted case with extremely inhomogeneous mixing. This result was verified by
69 Slawinska et al. (2008) using a large-eddy simulation (LES) model. Although the
70 influence of different mixing mechanisms in simulations is lower when two-moment
71 microphysics schemes are used (Hill et al., 2009; Grabowski and Morrison, 2011;
72 Slawinska et al., 2012; Xu et al., 2020), Hill et al. (2009) also claimed that there are
73 still many uncertainties in the entrainment-mixing process, and the effect of different
74 mixing mechanisms can be more important over the entire cloud life-cycle.

75 In recent years, methods have been developed to describe general entrainment-
76 mixing processes, with homogeneous and extremely inhomogeneous scenarios as
77 special cases (Andrejczuk et al., 2006; Andrejczuk et al., 2009; Lehmann et al., 2009;
78 Lu et al., 2011). Hoffmann et al. (2019) and Hoffmann and Feingold (2019) conducted
79 LES at the subgrid-scale with turbulent mixing, using a linear eddy model. Andrejczuk

80 et al. (2009) used the results of direct numerical simulation (DNS) to establish a
81 relationship between instantaneous microphysical properties and Damköhler number
82 (D_a , Burnet and Brenguier, 2007), and developed a parameterization of the entrainment-
83 mixing process. Lu et al. (2013) developed a parameterization of the entrainment-
84 mixing process based on the relationship between the homogeneous mixing degree (ψ)
85 and transition scale number (N_L) in the explicit mixing parcel model (EMPM), as well
86 as aircraft observation data. Gao et al. (2018) investigated how ψ is related to D_a and
87 N_L in a DNS, to improve the parameterization of the entrainment-mixing process. Luo
88 et al. (2020) simulated more than 12,000 cases with EMPM by changing a variety of
89 parameters affecting entrainment-mixing processes and developed a parameterization
90 that improved the one proposed by Lu et al. (2013).

91 Although several entrainment-mixing parametrizations have been proposed, to the
92 best of our knowledge, only one study (Jarecka et al., 2013) has coupled an entrainment-
93 mixing parameterization with cloud microphysics to consider the change in cloud
94 droplet concentration during the entrainment-mixing process. Jarecka et al. (2013)
95 applied an entrainment-mixing parameterization, in terms of the Damköhler number, to
96 a two-moment microphysics scheme and found small impacts of entrainment-mixing
97 parameterization in shallow cumulus clouds. To further explore the influences of
98 entrainment-mixing processes, this study first modifies the entrainment-mixing
99 parameterization in terms of the transition scale number proposed by Luo et al. (2020)
100 to couple it more easily with microphysics schemes. The parameterization is then

101 implemented in the two-moment Thompson aerosol-aware scheme (Thompson and
102 Eidhammer, 2014). Finally, the effects of parameterization on the physical properties
103 of clouds are examined in both cumulus and stratocumulus clouds.

104 The rest of this paper is organized as follows: Section 2 describes the new
105 entrainment-mixing parameterization, simulated cases, and modelling setup. The major
106 results are presented and discussed in Section 3. The influences of the new entrainment-
107 mixing parameterization on cloud physics and the underlying mechanisms are
108 examined, and the effects of turbulence dissipation rate (ϵ) and aerosol concentration
109 are also discussed. Some concluding remarks are presented in Section 4.

110

111 **2. Parameterization, simulated cases, and modeling setup**

112 **2.1 The new entrainment-mixing parameterization**

113 According to Morrison and Grabowski (2008), the effect of the entrainment-
114 mixing process on cloud microphysical properties can be expressed as follows:

$$115 \quad N_c = N_{c0} \left(\frac{q_c}{q_{c0}} \right)^\alpha, \quad (1)$$

116 where N_c and N_{c0} are the cloud droplet number concentrations after and before the
117 evaporation process, respectively, and q_c and q_{c0} represent the corresponding cloud
118 water mixing ratios. It is noteworthy that when a new saturation is achieved after
119 evaporation, q_c is determined by q_{c0} , relative humidity (RH), air pressure, and
120 temperature. The parameter α can be pre-set to any value between 0 (homogeneous
121 mixing) and 1 (extremely inhomogeneous mixing) to represent a different degree of

122 subgrid-scale mixing homogeneity. In this study, instead of specifying α as a
 123 predetermined constant, here it is determined through expressions (Lu et al., 2013; Luo
 124 et al., 2020)

$$125 \quad \alpha = 1 - \psi, \quad (2a)$$

$$126 \quad \psi = c \exp(aN_L^b). \quad (2b)$$

127 where a , b and c are the three fitting parameters (Luo et al., 2020). The dimensionless
 128 number N_L is a dynamical measure of the degree of subgrid-scale mixing homogeneity
 129 (Lu et al., 2011) defined by

$$130 \quad N_L = \frac{L^*}{\eta}, \quad (3a)$$

$$131 \quad \eta = (\nu^3 / \varepsilon)^{1/4}, \quad (3b)$$

$$132 \quad L^* = \varepsilon^{1/2} \tau_{\text{evap}}^{3/2}, \quad (3c)$$

133 where L^* is the transition length (Lehmann et al., 2009), η is the Kolmogorov microscale,
 134 ν is the kinematic viscosity; ε is calculated from the subgrid turbulent kinetic energy
 135 (Deardorff, 1980):

$$136 \quad \varepsilon = CE^{3/2} / L, \quad (4)$$

137 where $C = 0.70$ is an empirical constant, E is the subgrid turbulent kinetic energy, and
 138 L is the model grid size. The evaporation time scale (τ_{evap}) is defined as the time taken
 139 for droplets to evaporate completely in an unsaturated environment, and is calculated
 140 as

$$141 \quad \tau_{\text{evap}} = -\frac{r^2}{2AS_e}, \quad (5a)$$

142
$$A = \frac{1}{\left[\left(\frac{L_h}{R_v T} - 1 \right) \frac{L_h \rho_L}{KT} + \frac{\rho_L R_v T}{D e_s(T)} \right]}, \quad (5b)$$

143 where r is the volume-mean radius of cloud droplets, A is a function of pressure and
 144 temperature, S_e is the supersaturation (RH-1) of entrained air, L_h is the latent heat, R_v is
 145 the specific gas constant for water vapour, T is air temperature, ρ_L is the density of liquid
 146 water, K is the coefficient of thermal conductivity of air, D is the diffusion coefficient
 147 of water vapour in the air, and $e_s(T)$ is the saturation vapour pressure over a plane water
 148 surface at temperature T .

149 Unfortunately, S_e in Equation (5a) is generally unavailable in atmospheric models,
 150 including LES models. Thus, the entrainment-mixing parameterization developed by
 151 Luo et al. (2020) based on the properties of entrained air cannot be used directly. To
 152 solve this problem, we modify the entrainment-mixing parameterization of Luo et al.
 153 (2020) by replacing S_e with the domain-mean RH in the EMPM, after entrainment but
 154 before evaporation, based on 12,218 cases:

155
$$\psi = 107.19 \exp(-1.99 N_L^{-0.29}). \quad (6)$$

156 Figure 1 shows the fitting results of the modified new entrainment-mixing
 157 parameterization. Compared to the parametrization proposed by Luo et al. (2020), the
 158 modified parameterization has similar ψ - N_L distributions, but with a larger N_L for the
 159 same ψ , because the EMPM domain-mean RH is larger than the entrained air RH. With
 160 this modification, N_L , ψ , and thus the effect of the entrainment-mixing processes on
 161 droplet concentration can be directly calculated using the LES grid-mean RH. It is

162 important to note that the parameterization does not mean that the entrained air RH is
163 equal to that of the LES grid-mean RH. It is also worth noting that a wide range of ε ,
164 S_e , and fraction of entrained air (f) are taken into account when establishing the
165 parameterization with the EMPM. The details of the EMPM simulations and related
166 calculations are provided by Luo et al. (2020).

167

168 **2.2 LES model, simulation cases, and modelling setup**

169 The LES model is built by applying the large-scale forcing module presented in
170 Endo et al. (2015) to the Weather Research and Forecasting (WRF) model tailored for
171 solar irradiance forecasting (WRF-Solar, Hacker et al., 2016; Haupt et al., 2016). The
172 large-scale forcing data (VARANAL) used in this process is derived from the
173 constrained variational analysis (CVA) approach developed by Zhang et al. (2001) and
174 provided by the U.S. Department of Energy’s Atmospheric Radiation Measurement
175 Program (www.arm.gov). The modified entrainment-mixing parameterization is
176 implemented in the two-moment Thompson aerosol-aware scheme (Thompson and
177 Eidhammer, 2014).

178 To investigate the behaviours of the new entrainment-mixing parameterization in
179 different cloud types, cumulus and stratocumulus cases are simulated. For both the
180 cumulus and stratocumulus cases, the horizontal resolution of the model is $100\text{ m} \times 100$
181 m with a domain area of $14.4\text{ km} \times 14.4\text{ km}$. The vertical direction is divided into 225
182 layers with a resolution of 30 m.

183 For each cloud case, ψ is first set to 1 for the *default* experiment because most LES
184 models assume a homogeneous entrainment-mixing mechanism. The simulation with
185 the new entrainment-mixing parameterization (Equations (1-6)) is hereafter referred to
186 as *new*. First, N_L is diagnosed for each grid, and ψ is then calculated using Equation (6).
187 Finally, the variation in N_c during entrainment-mixing is obtained using Equations (1)
188 and (2a). To examine the influence of the aerosol number concentration on the
189 entrainment-mixing process, we conduct the numerical experiments *default_10* and
190 *new_10* by multiplying the initial aerosol number concentrations, for the *default* and
191 *new* models, respectively, by a factor of 10. Thus, four sets of numerical experiments
192 are conducted for both the cumulus and stratocumulus cases; the names of the
193 experiments and corresponding descriptions are summarized in Table 1.

194

195 **3. Results**

196 **3.1 Cumulus case**

197 For the cumulus case, the simulation starts at 12:00 UTC on 11 June 2016 and
198 ends at 03:00 UTC on 12 June 2016 with an output interval of 10 min and spin-times
199 of 3 h. To demonstrate the utility of the model, Figure 2 compares the temporal
200 evolution of the observed and simulated cloud fraction (a) and solar irradiance (b) from
201 the *default* experiment. Grid points with q_c larger than 0.01 g/kg are defined as “cloudy
202 areas”. Also shown for comparison is observational data with a one-hour temporal
203 resolution, which is provided by the LES Atmospheric Radiation Measurement

204 Symbiotic Simulation and Observation (LASSO) campaign (Gustafson et al., 2020).
 205 The observations show that the cloud forms at 12:00 UTC on 11 June and dissipates
 206 completely by 01:00 UTC on 12 June with a maximum cloud fraction of 0.47 at 16:00
 207 UTC on 11 June. Considering the difference between the solar irradiances obtained
 208 from point measurements and the value representing the simulation domain, the
 209 observed solar irradiance at the Southern Great Plains (SGP) Central Facility are
 210 compared with the results of central grid point in simulation (Figure 2(b)). Evidently,
 211 although the results of simulation do not fluctuate as much as the observations, the
 212 model captures the general behaviours of both cloud fraction and solar irradiance. The
 213 general agreement between the simulations and observations lends credence to using
 214 the model in further study.

215 Figure 3 shows the evolution of the microphysical and optical properties of clouds
 216 in the cloudy areas of all simulation experiments, including q_c , N_c , droplet volume-
 217 mean radius (r_v), cloud water path (CWP), and cloud optical depth (τ). To visually and
 218 simultaneously compare the change in cloud droplet concentration under different
 219 aerosol concentrations, the maximum cloud droplet concentration (N_{cmax}) from *default*
 220 is used to normalize N_c in *default* and *new*, while N_{cmax} from *new_10* is used to
 221 normalize N_c in *default_10* and *new_10*. The CWP is calculated as:

$$222 \quad \text{CWP} = \int_0^H \rho_a q_c(z) dz, \quad (7)$$

223 where ρ_a is the air density, $q_c(z)$ is the cloud water mixing ratio at each height (z), and
 224 H is the cloud thickness. The optical depth τ is estimated with

225
$$\tau = \frac{3}{2} \frac{1}{\rho_w} \int_0^H \frac{\rho_a q_c(z)}{r_e(z)} dz, \quad (8)$$

226 where ρ_w is the water density and $r_e(z)$ is the effective radius of the cloud droplets at
 227 each height (z). The time-averaged values of these physical properties of the clouds are
 228 listed in Table 2 for convenience.

229 For the low aerosol number concentration, the simulations with the new
 230 entrainment-mixing parameterization have smaller N_c (35.53 cm^{-3}) and larger r_v (13.29
 231 μm) than the default homogeneous simulation (35.78 cm^{-3} for N_c and $13.27 \mu\text{m}$ for r_v
 232 in *default*). However, comparing *new* to *default*, the relative changes in N_c , r_v , and τ are
 233 very small. When the aerosol concentration increases ten-fold (*default_10* and *new_10*),
 234 q_c , CWP, and τ increase according to the aerosol indirect effect (Peng et al., 2002; Wang
 235 et al., 2019; Li et al., 2011; Wang et al., 2011). Meanwhile, r_v decreases significantly
 236 owing to the larger cloud number concentration. The effects of the new entrainment-
 237 mixing parameterization also increase, for example, the change in N_c increases from $-$
 238 0.70% (*new* compared to *default*) to -2.74% (*new_10* compared to *default_10*), r_v
 239 increases from $+0.15\%$ to $+0.57\%$, and τ from -0.38% to -0.58% ; the reasons for these
 240 changes are discussed later. These small changes are similar to those identified in
 241 previous cumulus studies (Jarecka et al., 2013; Hoffmann et al., 2019).

242

243 **3.2 Stratocumulus case**

244 The stratocumulus case is simulated from 9:00 UTC on 19 April 2009 to 03:00
 245 UTC on 20 April 2009; the first three hours are set to be spin-up times. We examine the

246 stratocumulus region of the cloud base at ~ 2.1 km and the cloud top at ~ 2.3 km (cloud
247 thickness of ~ 200 m). Figure 4 shows the time series of the domain-averaged cloud
248 fraction and total downward irradiance at the central point in the observation and the
249 *default* experiment from 12:00 UTC to 24:00 UTC. Similar to the cumulus case, the
250 simulations compare favourably with the observations, which further reinforces the
251 utility of the LES model. The observed data show that the cloud fraction increases with
252 time and peaks at 16:00 UTC. The simulated cloud fraction has a value of 1 before
253 16:00 UTC, fluctuates from 16:00 UTC to 21:00 UTC, and decreases sharply after
254 21:00 UTC. This period can be divided into three stages, namely the mature stage, pre-
255 dissipation stage, and dissipation stage.

256 As with the cumulus case, the temporal evolutions of the physical properties (q_c ,
257 N_c , r_v , CWP, and τ) of the clouds are shown in Figure 5. In contrast to the oscillating
258 changes exhibited by the physical quantities in the cumulus case (Figure 3), the physical
259 properties in the stratocumulus case exhibit a mostly smooth temporal evolution.
260 Furthermore, *default* and *new* exhibit clear distinctions during the early periods, but
261 these differences decrease during the dissipation stage. This is also the case with
262 *default_10* and *new_10*.

263 To compare the different behaviours of the simulation experiments at different
264 stages, the results at the mature and dissipation stages are analysed in detail. The mean
265 values of the main microphysical and optical properties of the clouds are summarised
266 in Table 3. As expected, the cloud microphysical and optical properties at the mature

267 stage are all larger than those at the dissipation stage. The effects of the new
268 entrainment-mixing parametrization are also more significant at the mature stage.
269 Compared to *default*, the *new* model results in a 7.36% smaller N_c , 3.20% larger r_v , and
270 5.98% smaller τ during the mature stage. During the dissipation stage, the changes in
271 N_c , r_v , and τ are -4.76% , $+2.12\%$, and -2.56% , respectively. The largest influence of
272 the new entrainment-mixing parametrization occurs during the mature stage when the
273 aerosol concentration is ten times greater. The differences in N_c , r_v , and τ between
274 *new_10* and *default_10* are -9.69% , $+3.88\%$, and -5.85% , respectively, averaged over
275 the mature stage. These differences are much larger than those reported by Hill et al.
276 (2009) who found that assuming extremely inhomogeneous mixing has a negligible
277 effect on stratocumulus simulations. Our results also prove the speculation of Hill et al.
278 (2009) that the mixing process might play an important role when the stratocumulus is
279 thin (~ 200 m in this study). Furthermore, implementing the new entrainment-mixing
280 parameterization has similar effects on cloud properties to those described by Hoffmann
281 and Feingold (2019) who used the linear eddy model to represent subgrid-scale
282 turbulent mixing. Note that stratocumulus clouds occur in most regions around the
283 world and are important contributors to the surface radiation budget (Wood, 2012;
284 Zheng et al., 2016; Wang et al., 2021; Wang and Feingold, 2009). Stratocumulus clouds
285 dominate in some regions and occur over 60% of the time as vast long-lived sheets,
286 such as the *semi-permanent subtropical marine stratocumulus sheets* (Wood, 2012). In
287 these regions, a nearly 6% decrease in τ , caused by the new entrainment-mixing

288 parameterization is expected to have significant effects on the simulation of regional
289 radiative properties and climate change.

290 The averaged influences of the new entrainment-mixing parametrization over all
291 the simulation periods are also examined (Table 4). Quantitatively, the effect of the new
292 entrainment-mixing parameterization is much greater on stratocumulus clouds than on
293 cumulus clouds. Compared to *default*, *new* has an average change of -6.20% in N_c ,
294 $+2.01\%$ in r_v , and -3.23% in τ . When the aerosol concentration increases ten-fold, the
295 differences in N_c , r_v , and τ between *default_10* and *new_10* are -9.00% , $+3.16\%$, and
296 -4.14% , respectively. These differences are larger than the largest changes in the
297 cumulus case.

298

299 **3.3 Mechanisms of the effects of the new entrainment-mixing parameterization**

300 The different effects of the new entrainment-mixing parameterization on different
301 types of clouds and even on different stages of stratocumulus clouds are likely be related
302 to variations in the dominant mixing mechanism. To confirm this, we calculate the
303 average ψ at all grid points experiencing evaporation, the proportion of inhomogeneous
304 mixing grid points to all grid points experiencing evaporation, and the average ψ at the
305 inhomogeneous mixing grid points in *new* and *new_10* (Table 5) for the cumulus case,
306 and mature and dissipation stages in the stratocumulus case.

307 For the cumulus case, simulations exhibit large ψ and a small proportion of
308 inhomogeneous mixing, indicating that homogeneous mixing is the dominant

309 entrainment-mixing mechanism (Luo et al., 2020; Lu et al., 2013). Correspondingly,
310 the influences of the new entrainment-mixing parameterization on the cloud physical
311 properties are not significant, as shown in Figure 3 and Table 2. The *new_10* model
312 exhibit a smaller average ψ and a larger proportion of inhomogeneous mixing than *new*,
313 which results in larger changes in cloud physics, as mentioned in Section 3.1.

314 For the stratocumulus case, Table 5 shows the average ψ at all grid points
315 experiencing evaporation, the proportion of inhomogeneous mixing grid points to all
316 grid points experiencing evaporation, and the average ψ at the inhomogeneous mixing
317 grid points during the two stages. The mature stage always has a smaller ψ but a larger
318 proportion of inhomogeneous mixing than the dissipation stage. The inhomogeneous
319 mixing process dominates the mature stage in *new*, because more than 60% of the grid
320 points experience inhomogeneous mixing. The inhomogeneous mixing process is more
321 dominant in *new_10*, because less than 3% of the cloudy grid points experience a
322 homogeneous mixing process during the mature stage, which explains why *new_10* has
323 the largest influence when implementing the new entrainment-mixing parametrization.
324 Meanwhile, the average ψ in both stages is smaller than that in the cumulus case for the
325 same simulation configuration. Thus, the effects of the new entrainment-mixing
326 parameterization are more significant for stratocumulus than for cumulus clouds,
327 especially at the mature stage. It is noted that the average ψ and the proportion of
328 inhomogeneous mixing at the dissipation stage of *new* in the stratocumulus case are
329 very close to the results of *new_10* in the cumulus case. This is because the cloud

330 fraction decreases sharply during the dissipation stage; the stratocumulus clouds break
331 up and produces cumulus clouds with small cloud droplet radius.

332

333 **3.4 The effects of dissipation rate and aerosol concentration on the entrainment-** 334 **mixing process**

335 Previous studies have shown the notable effects of the dissipation rate and aerosol
336 concentration on the entrainment-mixing process. For example, Luo et al. (2020)
337 changed ε from $10^{-5} \text{ m}^2 \text{ s}^{-3}$ to $10^{-2} \text{ m}^2 \text{ s}^{-3}$ and noted huge differences in the corresponding
338 ψ . Small et al. (2013) compared aircraft observations with different background
339 concentrations and found that higher pollution flights tended to slightly more
340 inhomogeneous mixing; Jarecka et al. (2013) also showed various homogeneities of
341 subgrid mixing when aerosol concentration increases ten-fold. To explain the different
342 behaviours of different simulations with the new entrainment-mixing parameterization,
343 the influences of ε and aerosol concentration are examined. Figure 6 shows the
344 probability distribution functions (PDFs) of ε , r_v , τ_{evap} , and N_L for cloud grids
345 experiencing entrainment-mixing processes in *new* and *new_10* for the cumulus and
346 stratocumulus cases, respectively. The PDFs from the mature and dissipation stages of
347 the stratocumulus case are shown in Figure 7.

348

349 **3.4.1 Dissipation rate**

350 According to Equation (3), N_L is a function of $\varepsilon^{3/4}$; hence, the PDF of ε directly

351 affects N_L and further results in different ψ . For the cumulus case, the mean ε of 0.0043
352 $\text{m}^2 \text{s}^{-3}$ in *new* is similar to those obtained for cumulus clouds in previous studies (e.g.
353 Lu et al., 2016; Hoffmann et al., 2019). As shown in Figure 1, cloud grids experience a
354 homogeneous mixing process if N_L is larger than $\sim 10^5$, the limited distribution of N_L
355 values less than 10^5 in *new* results in a very small number of cloud grid points
356 undergoing inhomogeneous mixing process. Even at the cloud grid points that undergo
357 inhomogeneous mixing, the average ψ is large (98.62%), because most of the N_L values
358 are larger than 10^3 . Therefore, the cloud properties in *new* are close to those in *default*.

359 For the stratocumulus case, the mean value of ε ($2.9 \times 10^{-4} \text{m}^2 \text{s}^{-3}$ in *new*) is an order
360 of magnitude less than those in the cumulus case. Therefore, compared with the
361 cumulus case, N_L is reduced in the stratocumulus case, while the peak value of *new*
362 almost reaches the criterion of inhomogeneous mixing ($\sim 10^5$). For the two stages of
363 stratocumulus clouds, ε is an order of magnitude smaller, but r_v was larger (Figure 7)
364 during the mature stage than during the dissipation stage. According to Equation (5a),
365 droplets with smaller r_v are more prone to complete evaporation and have a smaller τ_{evap} .
366 The combination of smaller ε and larger r_v results in a smaller N_L (Equation (3)). This
367 is the reason for the new entrainment-mixing parametrization having more significant
368 effects during the mature stage than during the dissipation stage. In addition, the
369 similarity of the ε and r_v values during the dissipation stage of the stratocumulus case
370 in *new*, compared to the cumulus case in *new_10* (Figures 6a and 6b), explains the
371 similar average ψ values of these scenarios and the proportion of inhomogeneous

372 mixing (Table 5).

373 Therefore, the distribution of ε has a vital impact on the influence of the new
374 entrainment-mixing parameterization. Smaller values of ε result in the new
375 entrainment-mixing parameterization having a more significant influence. Moreover,
376 the r_v in the stratocumulus case is smaller than that in the cumulus case, which is also
377 conducive to a more inhomogeneous mixing process. These are the reasons why the
378 implementation of the new entrainment-mixing parameterization has a larger influence
379 in the stratocumulus case than in the cumulus case, when compared to a homogeneous
380 mixing mechanism.

381

382 **3.4.2 Aerosol concentration**

383 The aerosol concentration affects the entrainment-mixing process by decreasing
384 the cloud droplet radius. As r_v decreases, the distributions of τ_{evap} in *new_10* moves to
385 a smaller overall value, while the mean value is an order of magnitude smaller than that
386 in *new*, which causes a much smaller N_L because N_L is proportional to $\tau_{\text{evap}}^{3/2}$ (Equations
387 (3a) and (3b)). The larger percentage of smaller N_L values indicates that in *new_10*,
388 more grid points undergo an inhomogeneous mixing process, and the proportion of such
389 grid points is much larger than in the *new* model (Table 5). Therefore, compared to *new*,
390 *new_10* exhibit a smaller ψ and the effects of the new entrainment-mixing
391 parameterization on cloud properties are more obvious, for both the cumulus and
392 stratocumulus cases.

393

394 **3.5 Verification by the simulations with a different parameterization using**
395 **entrained air relative humidity**

396 In the above simulations, the new entrainment-mixing parameterization is based
397 on the grid-mean RH. This section serves to verify these simulations using the the
398 entrainment-mixing parameterization proposed by Luo et al. (2020)

399
$$\psi = 107.96 \exp(-0.95 N_L^{-0.35}), \quad (9)$$

400 which was developed using the entrained air RH in the EMPM. This parameterization
401 needs the entrained air RH within each grid in WRF, which is estimated following
402 Grabowski (2007) and Jarecka et al. (2009). Briefly, assuming that RH mixes linearly
403 when the dry air entrains into the cloud, then entrained air RH can be simply calculated
404 by

405
$$RH_{\text{entrained}} = \frac{RH_{\text{grid}} - (1 - f)RH_{\text{cloud}}}{f}, \quad (10)$$

406 where the subscripts *entrained*, *cloud*, and *grid* indicate the RH of the entrained, cloudy,
407 and grid point air, respectively. In Equation (10), although the cloudy air RH is
408 approximately 100% and grid-mean RH is predicted in the model, the entrained air
409 fraction *f* needs to be further parameterized. To obtain *f* at 100 m, a parameterization of
410 *f* is developed based on the simulations for both the cumulus and stratocumulus cases
411 with a higher resolution of 10 m; the other configurations are the same as those in the
412 experiment *default*. The 10 m-resolution simulation results are then averaged to the
413 resolution of 100 m. Following Xu and Randall (1996), “1 - *f*” can be fitted by the

414 function

$$415 \quad 1 - f = RH_{\text{grid}}^{\gamma} [1 - \exp(-\beta q_c)], \quad (11)$$

416 where γ and β are empirical parameters. Figure 8 shows that the parameterization with
417 $\gamma = 8.72$ and $\beta = 1.47 \times 10^4$ can well reproduce the simulated values of “ $1 - f$ ”, with the
418 correlation coefficient of 0.89 and significant level p -value < 0.01 .

419 Equations (9-11) are applied in the simulations for both the cumulus and
420 stratocumulus cases with different aerosol background (hereafter *new_f* and
421 *new_f_10*). Same as Figures 3 and 5, the temporal evolutions of the cloud physical
422 properties (q_c , N_c , r_v , CWP, and τ) in *default*, *default_10*, *new_f*, and *new_f_10* are
423 shown in Figures 9 and 10. The results are similar to Figures 3 and 5. The mean values
424 of these properties of *new_f* and *new_f_10* for the cumulus and stratocumulus cases
425 are also shown in Table 6, the results of *new* and *new_10* are also shown in the
426 parentheses for the convenience of comparison. The results of *new_f* and *new* are very
427 similar, with the maximum difference being no more than 1%, so are the results of
428 tenfold aerosol background. Such a close agreement suggests that the results of the
429 new entrainment-mixing parametrization with grid-mean RH are reliable.

430 It is worth noting that instead of parameterizing f , Jarecka et al. (2009) and
431 Jarecka et al. (2013) added an equation to predict f for each grid. In principle, this is a
432 good choice if this method is available in models.

433

434

435

436 **4. Concluding remarks**

437 The entrainment-mixing process near cloud edges has important effects on cloud
438 microphysics, but the most commonly used microphysics schemes simply assume one
439 extreme mechanism, that is, homogeneous entrainment-mixing. This study first
440 improves the entrainment-mixing parameterization proposed by Luo et al. (2020),
441 which connects the homogeneous mixing degree and transition scale number to
442 estimate the homogeneity of the subgrid mixing process and its impact on the droplet
443 number concentration. The improved parameterization uses grid-mean relative
444 humidity and can be implemented directly into microphysics schemes; there is no need
445 to know the relative humidity of the entrained air. Second, the modified entrainment-
446 mixing parameterization is implemented in the two-moment Thompson aerosol-aware
447 scheme of the LES version of WRF-Solar, to examine its effects on the microphysical
448 and optical properties of cumulus and stratocumulus clouds. Third, several sensitivity
449 experiments are conducted to investigate the effects of the new entrainment-mixing
450 parameterization under different conditions of turbulence dissipation rate and aerosol
451 number concentration. The results of implementing the new entrainment-mixing
452 parameterization are finally verified by the results using entrained air properties.

453 Unlike the commonly assumed homogeneous mixing scenario, the new
454 entrainment-mixing parameterization produces a smaller cloud droplet number
455 concentration and larger cloud droplet radius, with the degree of difference depending
456 on cloud types and stages. Sensitivity tests show that in the cumulus case, the largest

457 average influence of the new entrainment-mixing parameterization occurs under a high
458 aerosol background, but results in only a 2.74% decrease in cloud droplet number
459 concentration and a 0.57% increase in cloud droplet volume-mean radius. The changes
460 become even smaller with a low aerosol background because of the larger cloud droplet
461 radius. In contrast, the new entrainment-mixing parameterization has a larger influence
462 on the microphysical and optical properties of stratocumulus clouds, especially under a
463 high aerosol background and during the mature stage, with a cloud fraction equal to 1.
464 The largest changes resulting from the new entrainment-mixing parameterization are –
465 9.69%, +3.88%, and –5.85%, for cloud number concentration, cloud droplet volume-
466 mean radius, and cloud optical depth, respectively. The new entrainment-mixing
467 parameterization has less of an influence on the dissipation stage than on the mature
468 stage of the stratocumulus case, but affects this case more than the cumulus case.

469 The varying effects of the new entrainment-mixing parameterization are caused
470 by variations in the dominant entrainment-mixing mechanism between different cloud
471 types and stages. Compared to the cumulus case, the stratocumulus case has a much
472 smaller homogeneous mixing degree and a larger proportion of inhomogeneous mixing
473 grid points, especially during the mature stage, which indicates that the inhomogeneous
474 mixing mechanism dominates in the stratocumulus case, while the homogeneous
475 mixing mechanism dominates in the cumulus case. As mentioned above, the changes
476 in physical properties of stratocumulus clouds in the dissipation stage are between those
477 in the mature stage and those of the cumulus case; this is because stratocumulus clouds

478 dissipate sharply to form small cumulus clouds, and the degree of homogeneous mixing
479 during the dissipation stage is therefore between that which occurs during the mature
480 stage and the cumulus case.

481 Sensitivity studies show that turbulence dissipation rate and aerosol concentration
482 can have notable effects on the subgrid homogeneity of the mixing process. A larger
483 dissipation rate can accelerate the mixing process, which results in a larger transition
484 scale number and homogeneous mixing degree; and therefore, a mostly homogenous
485 mixing mechanism. This is why the cumulus case exhibit smaller changes than the
486 stratocumulus case after the new entrainment-mixing parameterization is implemented.
487 Larger aerosol number concentrations cause a smaller cloud droplet radius. Smaller
488 droplets evaporate more easily, which leads to a smaller transition scale number and a
489 smaller homogeneous mixing degree. Thus, the entrainment-mixing mechanism tends
490 to be inhomogeneous. Therefore, a larger aerosol number concentration increases the
491 influence of the new entrainment-mixing parameterization in both the cumulus and
492 stratocumulus cases.

493 The influences of implementing the new entrainment-mixing parameterization
494 with grid-mean relative humidity have been verified by simulations with entrained air
495 properties. The entrained air properties are obtained and calculated from simulations
496 with a finer resolution (10 m). Sensitivity tests show similar cloud microphysical and
497 optical properties in the two different methods, which suggests that the new
498 entrainment-mixing parameterization with grid-mean relative humidity is convincing.

499 Note that the new entrainment-mixing parameterization could be more important
500 in the models if the relative humidity near the cloud is more accurately simulated,
501 because numerical diffusion may spuriously humidify the entrained air (Hoffmann and
502 Feingold, 2019). The artificially increased relative humidity limits the influences of the
503 new entrainment-mixing parameterization, because homogeneous and inhomogeneous
504 entrainment-mixing processes are close to each other under conditions of high relative
505 humidity.

506

507 **Author contributions.** XX, CL and YL designed the experiments. XX carried out the
508 experiments and conducted the data analysis with contributions from all coauthors. XX,
509 CL, XZ, and SE developed the model code. XX prepared the paper with help from CL,
510 YL, YW, SL, and LZ.

511

512 **Competing interests.** The authors declare that they have no conflict of interest.

513

514 **Acknowledgements.** This research is supported by the National Key Research and
515 Development Program of China (2017YFA0604001), the National Natural Science
516 Foundation of China (41822504, 42175099, 42027804, 41975181, 42075073). Liu,
517 Zhou, and Endo are supported by the U.S. Department of Energy's Office of Energy
518 Efficiency and Renewable Energy (EERE) under Solar Energy Technologies Office
519 (SETO) Award Number 33504, and Office of Science Biological and Environmental

520 Research as part of the Atmospheric Systems Research (ASR) Program. Brookhaven
521 National Laboratory is operated by Battelle for the U.S. Department of Energy under
522 Contract DE-SC00112704. The large-scale forcing data used in this paper can be
523 downloaded from the U.S. Department of Energy's Atmospheric Radiation
524 Measurement Program with <https://adc.arm.gov/discovery/#/results>. The LASSO data
525 can be downloaded from <https://archive.arm.gov/lassobrowser>. The views expressed
526 herein do not necessarily represent the views of the U.S. Department of Energy or the
527 United States Government.

528

529 **Reference**

- 530 Ackerman, A. S., Kirkpatrick, M. P., Stevens, D. E., and Toon, O. B.: The impact of
531 humidity above stratiform clouds on indirect aerosol climate forcing, *Nature*, 432,
532 1014-1017, 2004.
- 533 Andrejczuk, M., Grabowski, W. W., Malinowski, S. P., and Smolarkiewicz, P. K.:
534 Numerical simulation of cloud-clear air interfacial mixing: Effects on cloud
535 microphysics, *J. Atmos. Sci.*, 63, 3204-3225, doi:10.1175/JAS3813.1, 2006.
- 536 Andrejczuk, M., Grabowski, W. W., Malinowski, S. P., and Smolarkiewicz, P. K.:
537 Numerical simulation of cloud-clear air interfacial mixing: Homogeneous versus
538 inhomogeneous mixing, *J. Atmos. Sci.*, 66, 2493-2500, doi:10.1175/2009JAS2956.1,
539 2009.
- 540 Burnet, F. and Brenguier, J. L.: Observational study of the entrainment-mixing process
541 in warm convective clouds, *J. Atmos. Sci.*, 64, 1995-2011, doi:10.1175/JAS3928.1,
542 2007.
- 543 Chosson, F., Brenguier, J.-L., and Schüller, L.: Entrainment-mixing and radiative
544 transfer simulation in boundary layer clouds, *J. Atmos. Sci.*, 64, 2670-2682,
545 doi:10.1175/JAS3975.1, 2007.
- 546 Deardorff, J.: Stratocumulus-capped mixed layers derived from a three-dimensional
547 model, *Boundary-Layer Meteorol*, 18, 495-527, 10.1007/BF00119502, 1980.
- 548 Del Genio, A. D. and Wu, J.: The role of entrainment in the diurnal cycle of continental
549 convection, *J. Climate*, 23, 2722-2738, doi: 10.1175/2009JCLI3340.1, 2010.
- 550 Endo, S., Fridlind, A. M., Lin, W., Vogelmann, A. M., Toto, T., Ackerman, A. S.,
551 McFarquhar, G. M., Jackson, R. C., Jonsson, H. H., and Liu, Y.: RACORO continental

552 boundary layer cloud investigations: 2. Large - eddy simulations of cumulus clouds
553 and evaluation with in situ and ground - based observations, *Journal of Geophysical*
554 *Research: Atmospheres*, 120, 5993-6014, 2015.

555 Fan, J., Wang, Y., Rosenfeld, D., and Liu, X.: Review of Aerosol–Cloud Interactions:
556 Mechanisms, Significance, and Challenges, *Journal of the Atmospheric Sciences*, 73,
557 4221-4252, 10.1175/jas-d-16-0037.1, 2016.

558 Freud, E., Rosenfeld, D., and Kulkarni, J. R.: Resolving both entrainment-mixing and
559 number of activated CCN in deep convective clouds, *Atmos. Chem. Phys.*, 11, 12887-
560 12900, 2011.

561 Freud, E., Rosenfeld, D., Andreae, M. O., Costa, A. A., and Artaxo, P.: Robust relations
562 between CCN and the vertical evolution of cloud drop size distribution in deep
563 convective clouds, *Atmos. Chem. Phys.*, 8, 1661-1675, 2008.

564 Gao, S., Lu, C., Liu, Y., Mei, F., Wang, J., Zhu, L., and Yan, S.: Contrasting Scale
565 Dependence of Entrainment - Mixing Mechanisms in Stratocumulus Clouds,
566 *Geophysical Research Letters*, 47, 10.1029/2020gl086970, 2020.

567 Gao, S., Lu, C., Liu, Y., Yum, S. S., Zhu, J., Zhu, L., Desai, N., Ma, Y., and Wu, S.:
568 Comprehensive quantification of height dependence of entrainment mixing between
569 stratiform cloud top and environment, *Atmospheric Chemistry and Physics*, 21, 11225-
570 11241, 2021.

571 Gao, Z., Liu, Y., Li, X., and Lu, C.: Investigation of Turbulent Entrainment-Mixing
572 Processes with a New Particle-Resolved Direct Numerical Simulation Model, *J.*
573 *Geophys. Res.*, 123, 2194-2214, 2018.

574 Gerber, H. E., Frick, G. M., Jensen, J. B., and Hudson, J. G.: Entrainment, mixing, and
575 microphysics in trade-wind cumulus, *J. Meteorol. Soc. Japan*, 86A, 87-106, 2008.

576 Grabowski, W. W.: Indirect impact of atmospheric aerosols in idealized simulations of
577 convective-radiative quasi equilibrium, *J. Climate*, 19, 4664-4682,
578 doi:10.1175/JCLI3857.1, 2006.

579 Grabowski, W. W.: Representation of turbulent mixing and buoyancy reversal in bulk
580 cloud models, *Journal of the atmospheric sciences*, 64, 3666-3680, 2007.

581 Grabowski, W. W. and Morrison, H.: Indirect Impact of Atmospheric Aerosols in
582 Idealized Simulations of Convective–Radiative Quasi Equilibrium. Part II: Double-
583 Moment Microphysics, *Journal of Climate*, 24, 1897-1912, 10.1175/2010jcli3647.1,
584 2011.

585 Gustafson, W. I., Vogelmann, A. M., Li, Z., Cheng, X., Dumas, K. K., Endo, S., Johnson,
586 K. L., Krishna, B., Fairless, T., and Xiao, H.: The Large-Eddy Simulation (LES)
587 Atmospheric Radiation Measurement (ARM) Symbiotic Simulation and Observation
588 (LASSO) Activity for Continental Shallow Convection, *Bulletin of the American*
589 *Meteorological Society*, 101, E462-E479, 10.1175/bams-d-19-0065.1, 2020.

590 Hacker, J. P., Jimenez, P. A., Dudhia, J., Haupt, S. E., Ruiz-Arias, J. A., Gueymard, C.
591 A., Thompson, G., Eidhammer, T., and Deng, A.: WRF-Solar: Description and Clear-
592 Sky Assessment of an Augmented NWP Model for Solar Power Prediction, *Bulletin of*
593 *the American Meteorological Society*, 97, 1249-1264, 10.1175/bams-d-14-00279.1,

594 2016.

595 Haman, K. E., Malinowski, S. P., Kurowski, M. J., Gerber, H., and Brenguier, J.-L.:
596 Small scale mixing processes at the top of a marine stratocumulus - a case study, *Q. J.*
597 *Roy. Meteor. Soc.*, 133, 213-226, doi:10.1002/qj.5, 2007.

598 Haupt, S. E., Kosovic, B., Jensen, T., Lee, J., Jimenez, P., Lazo, J., Cowie, J.,
599 McCandless, T., Pearson, J., and Weiner, G.: The SunCast² solar-power forecasting
600 system: the results of the public-private-academic partnership to advance solar power
601 forecasting, National Center for Atmospheric Research (NCAR), Boulder (CO):
602 Research Applications Laboratory, Weather Systems and Assessment Program (US),
603 2016.

604 Hill, A. A., Feingold, G., and Jiang, H.: The influence of entrainment and mixing
605 assumption on aerosol-cloud interactions in marine stratocumulus, *J. Atmos. Sci.*, 66,
606 1450-1464, 2009.

607 Hoffmann, F. and Feingold, G.: Entrainment and mixing in stratocumulus: Effects of a
608 new explicit subgrid-scale scheme for large-eddy simulations with particle-based
609 microphysics, *J. Atmos. Sci.*, 76, 1955-1973, 10.1175/jas-d-18-0318.1, 2019.

610 Hoffmann, F., Yamaguchi, T., and Feingold, G.: Inhomogeneous mixing in Lagrangian
611 cloud models: Effects on the production of precipitation embryos, *Journal of the*
612 *Atmospheric Sciences*, 76, 113-133, 2019.

613 Huang, J., Lee, X., and Patton, E. G.: A modelling study of flux imbalance and the
614 influence of entrainment in the convective boundary layer, *Boundary-layer meteorology*,
615 127, 273-292, 2008.

616 Jarecka, D., Grabowski, W. W., and Pawlowska, H.: Modeling of Subgrid-Scale Mixing
617 in Large-Eddy Simulation of Shallow Convection, *Journal of the Atmospheric Sciences*,
618 66, 2125-2133, 10.1175/2009jas2929.1, 2009.

619 Jarecka, D., Grabowski, W. W., Morrison, H., and Pawlowska, H.: Homogeneity of the
620 subgrid-scale turbulent mixing in large-eddy simulation of shallow convection, *J.*
621 *Atmos. Sci.*, 70, 2751-2767, 2013.

622 Jensen, J. B., Austin, P. H., Baker, M. B., and Blyth, A. M.: Turbulent mixing, spectral
623 evolution and dynamics in a warm cumulus cloud, *J. Atmos. Sci.*, 42, 173-192,
624 doi:10.1175/1520-0469(1985)042<0173:TMSEAD>2.0.CO;2, 1985.

625 Kim, B.-G., Miller, M. A., Schwartz, S. E., Liu, Y., and Min, Q.: The role of adiabaticity
626 in the aerosol first indirect effect, *J. Geophys. Res.*, 113, D05210, doi:
627 10.1029/2007jd008961, 2008.

628 Kumar, B., Schumacher, J., and Shaw, R.: Cloud microphysical effects of turbulent
629 mixing and entrainment, *Theor. Comp. Fluid Dyn.*, 27, 361-376, 2013.

630 Lasher-Trapp, S. G., Cooper, W. A., and Blyth, A. M.: Broadening of droplet size
631 distributions from entrainment and mixing in a cumulus cloud, *Q. J. Roy. Meteor. Soc.*,
632 131, 195-220, doi:10.1256/qj.03.199, 2005.

633 Lehmann, K., Siebert, H., and Shaw, R. A.: Homogeneous and inhomogeneous mixing
634 in cumulus clouds: dependence on local turbulence structure, *J. Atmos. Sci.*, 66, 3641-
635 3659, doi:10.1175/2009JAS3012.1, 2009.

636 Li, Z., Li, C., Chen, H., Tsay, S. C., Holben, B., Huang, J., Li, B., Maring, H., Qian, Y.,
637 and Shi, G.: East Asian studies of tropospheric aerosols and their impact on regional
638 climate (EAST - AIRC): An overview, *Journal of Geophysical Research: Atmospheres*,
639 116, 2011.

640 Lu, C., Liu, Y., and Niu, S.: Examination of turbulent entrainment-mixing mechanisms
641 using a combined approach, *J. Geophys. Res.*, 116, D20207,
642 doi:10.1029/2011JD015944, 2011.

643 Lu, C., Liu, Y., Niu, S., and Endo, S.: Scale dependence of entrainment - mixing
644 mechanisms in cumulus clouds, *Journal of Geophysical Research: Atmospheres*, 119,
645 13,877-813,890, 2014.

646 Lu, C., Liu, Y., Niu, S., Krueger, S., and Wagner, T.: Exploring parameterization for
647 turbulent entrainment-mixing processes in clouds, *Journal of Geophysical Research:*
648 *Atmospheres*, 118, 185-194, 10.1029/2012jd018464, 2013.

649 Lu, C., Liu, Y., Zhang, G. J., Wu, X., Endo, S., Cao, L., Li, Y., and Guo, X.: Improving
650 parameterization of entrainment rate for shallow convection with aircraft measurements
651 and large eddy simulation, *J. Atmos. Sci.*, 73, 761-773, 10.1175/JAS-D-15-0050.1,
652 2016.

653 Luo, S., Lu, C., Liu, Y., Bian, J., Gao, W., Li, J., Xu, X., Gao, S., Yang, S., and Guo, X.:
654 Parameterizations of Entrainment - Mixing Mechanisms and Their Effects on Cloud
655 Droplet Spectral Width Based on Numerical Simulations, *Journal of Geophysical*
656 *Research: Atmospheres*, 125, e2020JD032972, 2020.

657 Morrison, H. and Grabowski, W. W.: Modeling supersaturation and subgrid-scale
658 mixing with two-moment bulk warm microphysics, *J. Atmos. Sci.*, 65, 792-812,
659 doi:10.1175/2007JAS2374.1, 2008.

660 Paluch, I. R. and Baumgardner, D. G.: Entrainment and fine-scale mixing in a
661 continental convective cloud, *J. Atmos. Sci.*, 46, 261-278, doi:10.1175/1520-
662 0469(1989)046<0261:EAFSMI>2.0.CO;2, 1989.

663 Pawlowska, H., Brenguier, J. L., and Burnet, F.: Microphysical properties of
664 stratocumulus clouds, *Atmos. Res.*, 55, 15-33, 2000.

665 Peng, Y., Lohmann, U., Leaitch, R., Banic, C., and Couture, M.: The cloud albedo-cloud
666 droplet effective radius relationship for clean and polluted clouds from RACE and
667 FIRE.ACE, *J. Geophys. Res.*, 107, AAC 1-1-AAC 1-6, 10.1029/2000JD000281, 2002.

668 Slawinska, J., Grabowski, W. W., Pawlowska, H., and Morrison, H.: Droplet activation
669 and mixing in large-eddy simulation of a shallow cumulus field, *J. Atmos. Sci.*, 69, 444-
670 462, 2012.

671 Slawinska, J., Grabowski, W. W., Pawlowska, H., and Wyszogrodzki, A. A.: Optical
672 properties of shallow convective clouds diagnosed from a bulk-microphysics large-
673 eddy simulation, *J. Climate*, 21, 1639-1647, 2008.

674 Small, J. D., Chuang, P., and Jonsson, H.: Microphysical imprint of entrainment in
675 warm cumulus, *Tellus B*, 65, 6647-6662, 2013.

676 Thompson, G. and Eidhammer, T.: A study of aerosol impacts on clouds and
677 precipitation development in a large winter cyclone, *Journal of the atmospheric*

678 sciences, 71, 3636-3658, 2014.

679 Wang, H. and Feingold, G.: Modeling mesoscale cellular structures and drizzle in
680 marine stratocumulus. Part I: Impact of drizzle on the formation and evolution of open
681 cells, *Journal of the Atmospheric Sciences*, 66, 3237-3256, 2009.

682 Wang, M., Ghan, S., Ovchinnikov, M., Liu, X., Easter, R., Kassianov, E., Qian, Y., and
683 Morrison, H.: Aerosol indirect effects in a multi-scale aerosol-climate model PNNL-
684 MMF, *Atmospheric Chemistry and Physics*, 11, 5431-5455, 2011.

685 Wang, Y., Zhao, C., McFarquhar, G. M., Wu, W., Reeves, M., and Li, J.: Dispersion of
686 Droplet Size Distributions in Supercooled Non - precipitating Stratocumulus from
687 Aircraft Observations Obtained during the Southern Ocean Cloud Radiation Aerosol
688 Transport Experimental Study, *Journal of Geophysical Research: Atmospheres*, 126,
689 e2020JD033720, 2021.

690 Wang, Y., Niu, S., Lv, J., Lu, C., Xu, X., Wang, Y., Ding, J., Zhang, H., Wang, T., and
691 Kang, B.: A new method for distinguishing unactivated particles in cloud condensation
692 nuclei measurements: Implications for aerosol indirect effect evaluation, *Geophysical*
693 *Research Letters*, 46, 14185-14194, 2019.

694 Wood, R.: Review: Stratocumulus Clouds, *Monthly Weather Review*, 140, 2373-2423,
695 2012.

696 Xu, K.-M. and Randall, D. A.: A semiempirical cloudiness parameterization for use in
697 climate models, *Journal of the atmospheric sciences*, 53, 3084-3102, 1996.

698 Xu, X., Sun, C., Lu, C., Liu, Y., Zhang, G. J., and Chen, Q.: Factors affecting
699 entrainment rate in deep convective clouds and parameterizations, *Journal of*
700 *Geophysical Research: Atmospheres*, 126, e2021JD034881, 2021.

701 Xu, X., Lu, C., Liu, Y., Gao, W., Wang, Y., Cheng, Y., Luo, S., and Van Weverberg, K.:
702 Effects of cloud liquid - phase microphysical processes in mixed - phase cumuli over
703 the Tibetan Plateau, *Journal of Geophysical Research: Atmospheres*, 125,
704 e2020JD033371, 2020.

705 Yang, B., Wang, M., Zhang, G. J., Guo, Z., Huang, A., Zhang, Y., and Qian, Y.: Linking
706 Deep and Shallow Convective Mass Fluxes via an Assumed Entrainment Distribution
707 in CAM5 - CLUBB: Parameterization and Simulated Precipitation Variability, *Journal*
708 *of Advances in Modeling Earth Systems*, 13, e2020MS002357, 2021.

709 Yang, F., Shaw, R., and Xue, H.: Conditions for super-adiabatic droplet growth after
710 entrainment mixing, *Atmos. Chem. Phys.*, 16, 9421-9433, 10.5194/acp-2016-94, 2016.

711 Yum, S.: Cloud droplet spectral broadening in warm clouds: An observational and
712 model study, Dissertation for the Doctoral Degree, University of Nevada, Reno, Nevada,
713 USA, 191 pp., 1998.

714 Zhang, M. H., Lin, J. L., Cederwall, R. T., Yio, J. J., and Xie, S. C.: Objective analysis
715 of ARM IOP data: Method and sensitivity, *Mon. Weather Rev.*, 129, 295-311,
716 10.1175/1520-0493(2001)129<0295:OAOAID>2.0.CO;2, 2001.

717 Zheng, Y. and Rosenfeld, D.: Linear relation between convective cloud base height and
718 updrafts and application to satellite retrievals, *Geophysical Research Letters*, 42, 6485-
719 6491, 10.1002/2015gl064809, 2015.

720 Zheng, Y., Rosenfeld, D., and Li, Z.: Quantifying cloud base updraft speeds of marine
721 stratocumulus from cloud top radiative cooling, *Geophysical Research Letters*, 43,
722 11,407-411,413, 2016.

723 Zhu, L., Lu, C., Yan, S., Liu, Y., Zhang, G. J., Mei, F., Zhu, B., Fast, J. D., Matthews,
724 A., and Pekour, M. S.: A New Approach for Simultaneous Estimation of Entrainment
725 and Detrainment Rates in Non - Precipitating Shallow Cumulus, *Geophysical Research*
726 *Letters*, 48, 10.1029/2021gl093817, 2021.

727

728

729 Table 1. Summary of names and corresponding descriptions of the four experiments for
 730 each case of cumulus and stratocumulus. The meaning of each symbol for each
 731 experiment can be found in the text.

	Entrainment-mixing parameterization	Dissipation rate	Aerosol number concentration
<i>default</i>	$\alpha = 0$	-	default
<i>new</i>	$\alpha = 1 - \psi,$ $\psi = 107.19 \exp(-1.99 N_L^{-0.29}).$	$\varepsilon = CE^{3/2} / L.$	default
<i>default_10</i>	$\alpha = 0$	-	default×10
<i>new_10</i>	$\alpha = 1 - \psi,$ $\psi = 107.19 \exp(-1.99 N_L^{-0.29}).$	$\varepsilon = CE^{3/2} / L.$	default×10

732

733 Table 2. Summary of the case mean values of the key quantities in all the simulations
 734 of the cumulus case, containing cloud water mixing ratio (q_c), cloud droplet number
 735 concentration (N_c), cloud droplet volume-mean radius (r_v), cloud water path (CWP),
 736 and cloud optical depth (τ). The experiments are detailed in Table 1.

	<i>default</i>	<i>new</i>	<i>default_10</i>	<i>new_10</i>
$q_c(\text{g/kg})$	0.44	0.44	0.56	0.57
$N_c(\text{cm}^{-3})$	35.78	35.53	278.80	271.16
$r_v(\mu\text{m})$	13.27	13.29	7.05	7.09
CWP(g/m^2)	142.30	144.25	186.52	187.13
τ	13.07	13.02	31.29	31.11

737

738

739 Table 3. Summary of the case mean values of the key quantities in all the simulations
740 of the stratocumulus case, including cloud water mixing ratio (q_c), cloud droplet number
741 concentration (N_c), cloud droplet volume-mean radius (r_v), cloud water path (CWP),
742 and cloud optical depth (τ). The numbers in and out of the parentheses are the results at
743 the mature and dissipation stages, respectively. The experiments are detailed in Table 1.

	<i>default</i>	<i>new</i>	<i>default_10</i>	<i>new_10</i>
$q_c(\text{g/kg})$	0.13 (0.039)	0.13 (0.039)	0.16 (0.041)	0.16 (0.041)
$N_c(\text{cm}^{-3})$	35.74 (19.76)	33.11 (18.82)	256.82 (138.74)	231.93 (126.90)
$r_v(\mu\text{m})$	10.32 (7.53)	10.65 (7.69)	5.15 (4.02)	5.35 (4.14)
CWP(g/m^2)	41.39 (2.57)	41.78 (2.43)	56.21 (2.71)	57.03 (2.77)
τ	4.68 (0.39)	4.40 (0.38)	13.17 (0.78)	12.40 (0.78)

744

745 Table 4. Cloud water mixing ratio (q_c), cloud droplet number concentration (N_c), cloud
746 droplet volume-mean radius (r_v), cloud water path (CWP), cloud optical depth (τ) in all
747 simulations for the entire lifetime of the stratocumulus case. The experiments are
748 detailed in Table 1.

	<i>default</i>	<i>new</i>	<i>default_10</i>	<i>new_10</i>
$q_c(\text{g/kg})$	0.11	0.11	0.13	0.13
$N_c(\text{cm}^{-3})$	29.98	28.12	223.65	203.50
$r_v(\mu\text{m})$	9.38	9.57	5.06	5.22
CWP(g/m^2)	30.78	29.92	42.22	43.13
τ	4.02	3.89	10.39	9.96

749

750

751 Table 5. Homogeneous mixing degree (ψ) at all grid points experiencing evaporation,
752 the proportion of inhomogeneous mixing grid points to all grid points experiencing
753 evaporation, and ψ at the inhomogeneous mixing grid points in the experiments *new*
754 and *new_10* (Table 1) for the cumulus (Cu) and stratocumulus (St) cases. The numbers
755 in and out of the parentheses are the results at the mature and dissipation stages in the
756 stratocumulus (St) case, respectively. The experiments are detailed in Table 1.

	ψ at all grids (%)	Proportion of inhomogeneous mixing grids (%)	ψ at the inhomogeneous mixing grids (%)
<i>new</i> (Cu)	99.93	4.52	98.62
<i>new_10</i> (Cu)	95.33	25.10	92.96
<i>new</i> (St)	78.56 (94.68)	63.07 (40.61)	71.56 (89.33)
<i>new_10</i> (St)	68.20 (88.11)	97.31 (73.54)	65.01 (84.99)

757

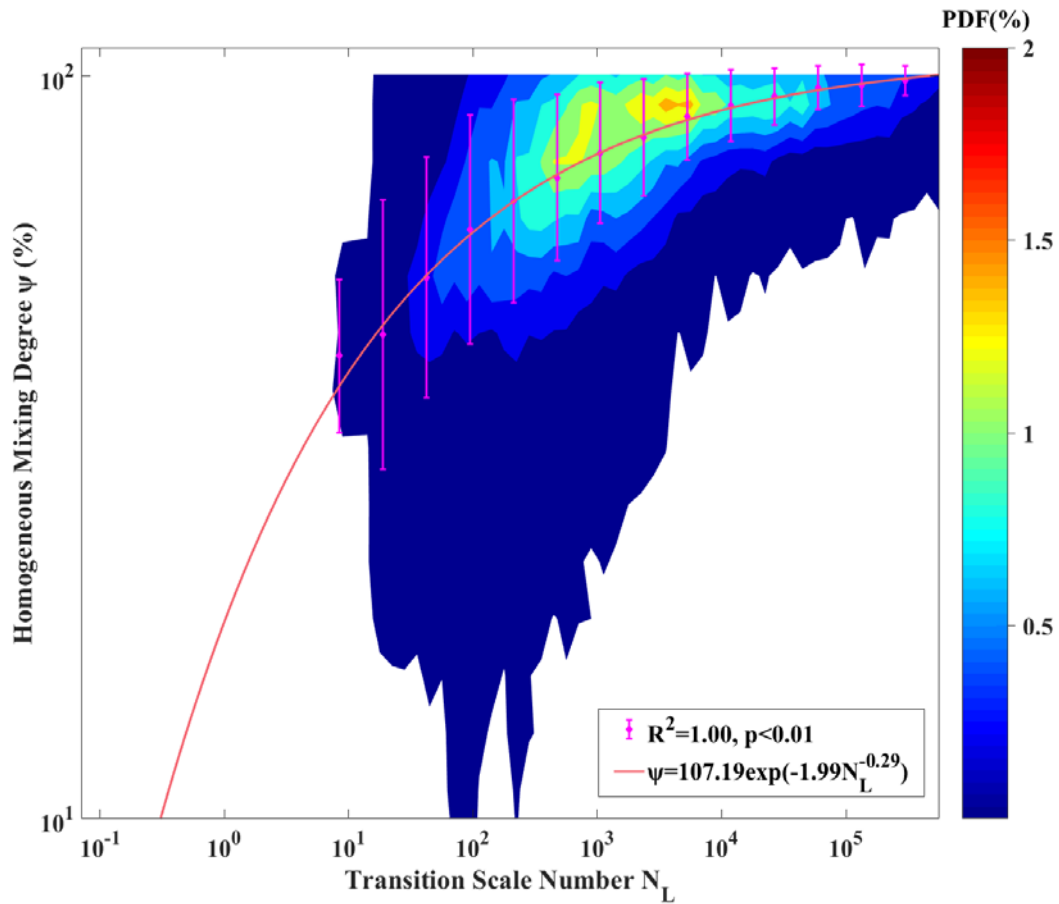
758

759 Table 6. Cloud water mixing ratio (q_c), cloud droplet number concentration (N_c), cloud
760 droplet volume-mean radius (r_v), cloud water path (CWP), cloud optical depth (τ) in
761 *new_f* and *new_f_10* for the cumulus (Cu) and stratocumulus (Sc) cases. The results of
762 *new* and *new_10* in Tables 2 and 4 are shown in the parentheses.

	Cu		Sc	
	<i>new_f</i>	<i>new_f_10</i>	<i>new_f</i>	<i>new_f_10</i>
	(<i>new</i>)	(<i>new_10</i>)	(<i>new</i>)	(<i>new_10</i>)
$q_c(\text{g/kg})$	0.44 (0.44)	0.57 (0.57)	0.11 (0.11)	0.13 (0.13)
$N_c(\text{cm}^{-3})$	35.52 (35.53)	270.56 (271.16)	28.08 (28.12)	202.99 (203.50)
$r_v(\mu\text{m})$	13.30 (13.29)	7.10 (7.09)	9.60 (9.57)	5.21 (5.22)
CWP(g/m^2)	143.15 (144.25)	185.95 (187.13)	30.16 (29.92)	43.32 (43.13)
τ	13.00 (13.02)	31.08 (31.11)	3.89 (3.89)	9.93 (9.96)

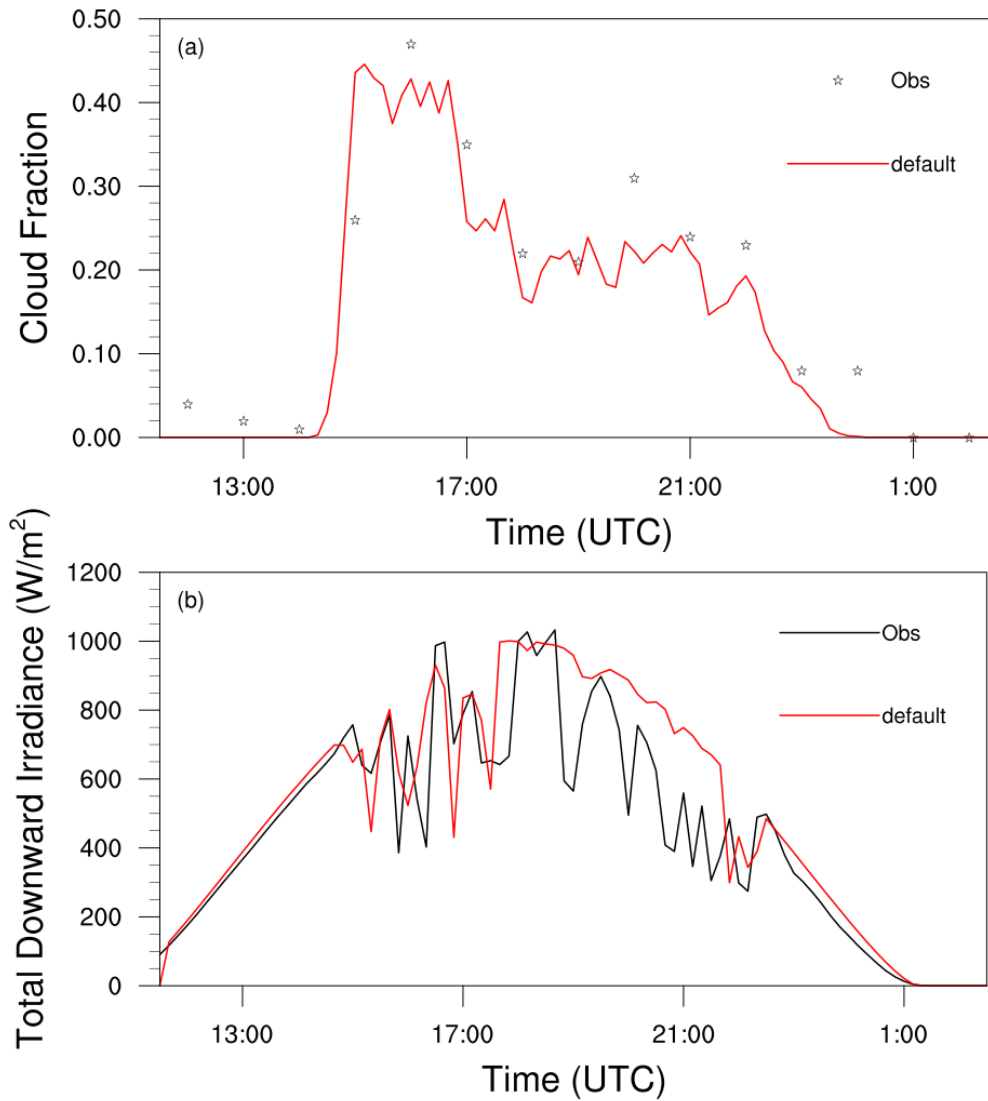
763

764



765

766 Figure 1. Parameterization of cloud entrainment-mixing mechanisms by relating
 767 homogeneous mixing degree (ψ) to transition scale number (N_L) from EMPM. The
 768 contours represent the joint probability distribution function (PDF) of ψ vs N_L . The
 769 magenta dots and error bars are mean values and standard deviations of ψ in each N_L
 770 bin, respectively. The mean values are fitted using a weighted least squares method with
 771 the number of data points in each N_L bin as the weight. The fitting equation, coefficient
 772 of determination (R^2), and p -value are also given. N_L is calculated by with the domain-
 773 averaged relative humidity after entrainment but before evaporation in the EMPM.



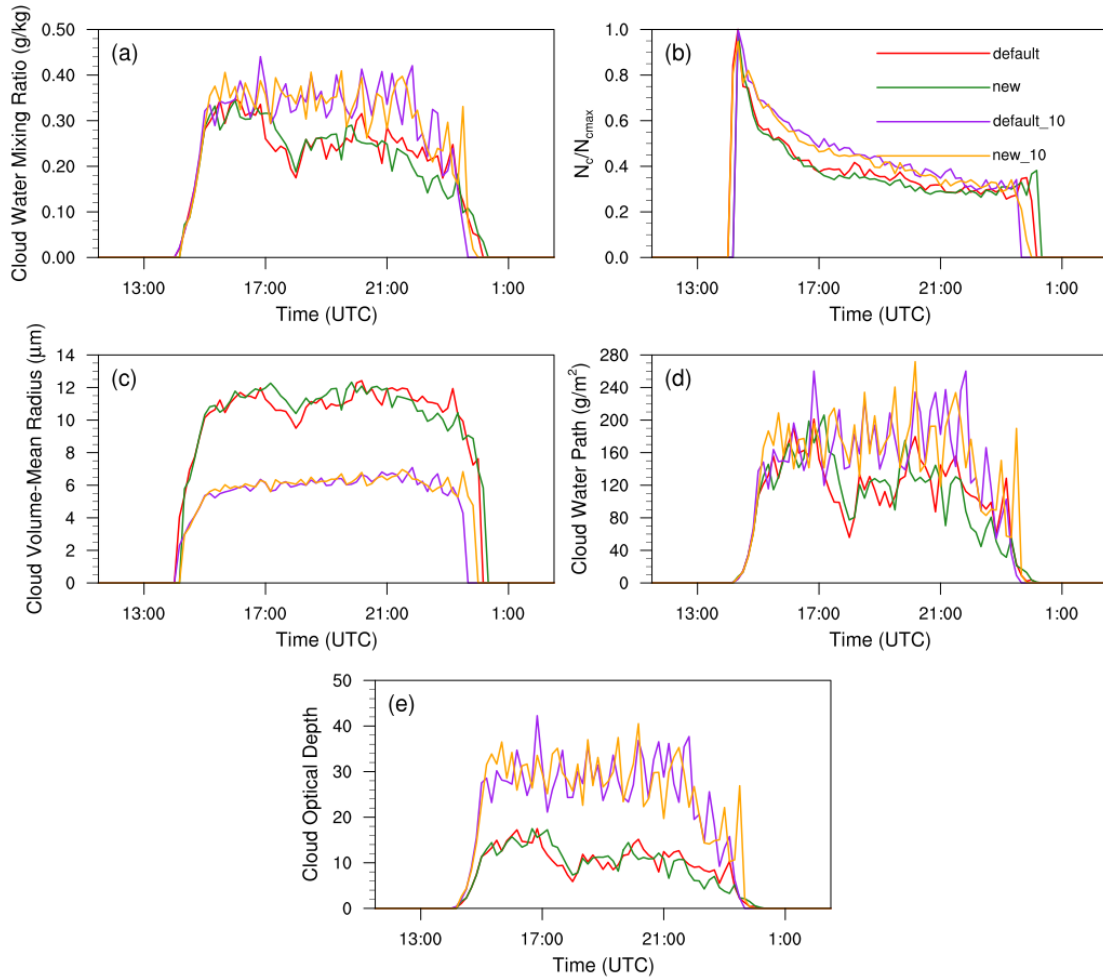
774

775 Figure 2. Time series of (a) domain-averaged cloud fraction and (b) total downward

776 irradiance at the central point from the observation and the *default* experiment in the

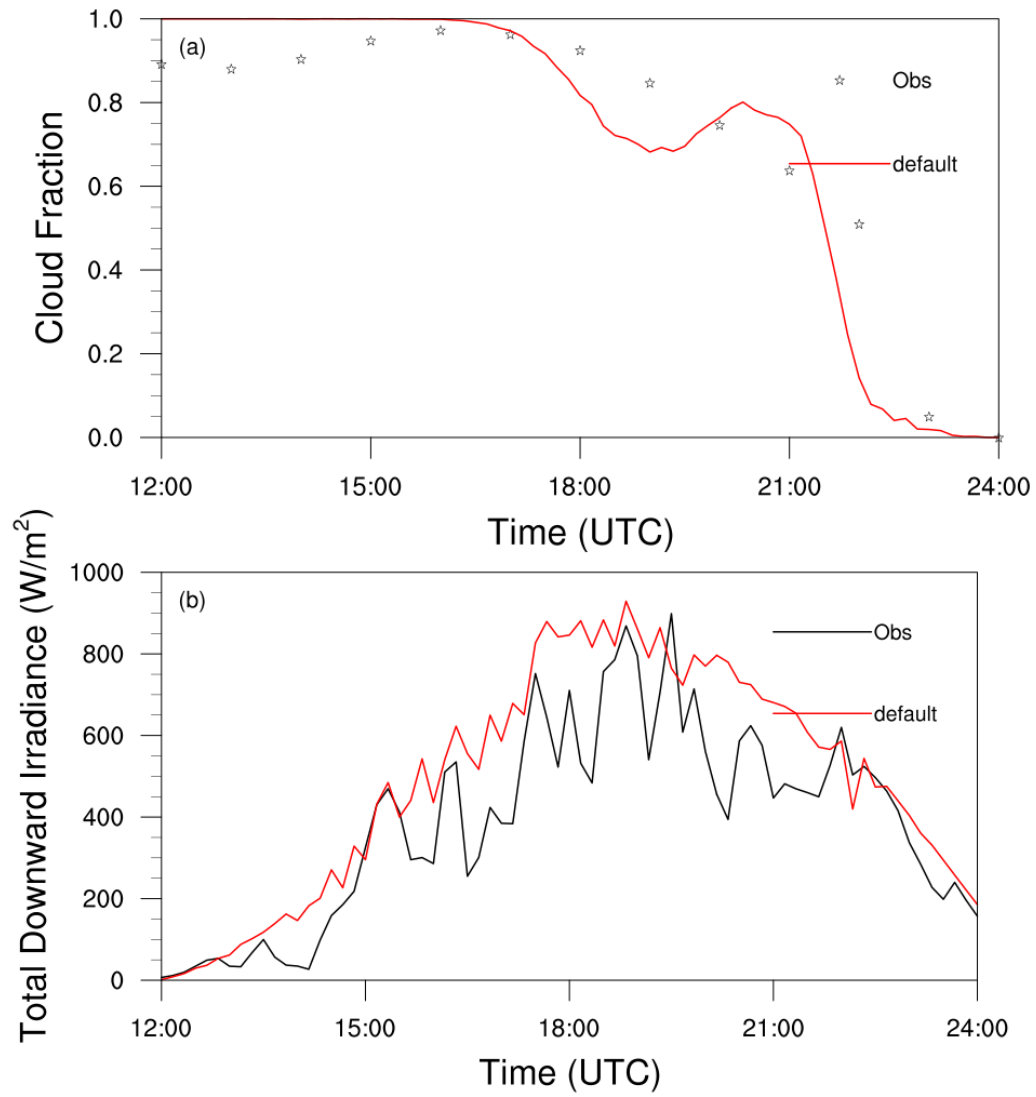
777 cumulus case.

778



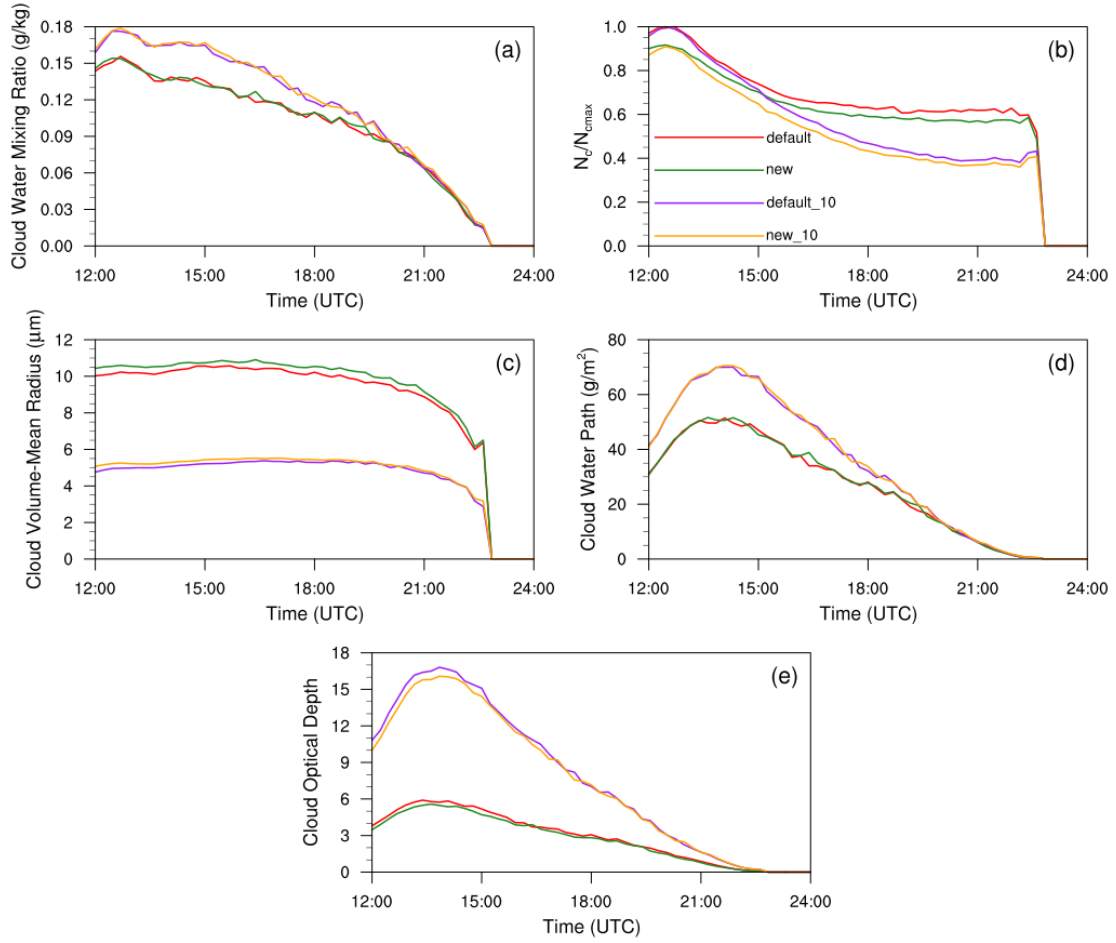
779

780 Figure 3. The temporal evolutions of main cloud microphysical and optical properties
 781 in all simulation experiments for the cumulus case, including (a) cloud water mixing
 782 ratio (q_c) (g/kg), (b) cloud droplet number concentration (N_c) (/cm³), (c) cloud droplet
 783 volume-mean radius (r_v) (μm), (d) cloud water path (CWP) (g/m²), and (e) cloud optical
 784 depth (τ). In (b), N_c in the experiments *default* and *new* are normalized by the maximum
 785 cloud droplet concentration (N_{cmax}) from *default*, respectively; N_c in the experiments
 786 *default_10* and *new_10* are normalized by N_{cmax} from *default_10*, respectively. The four
 787 experiments are detailed in Table 1.



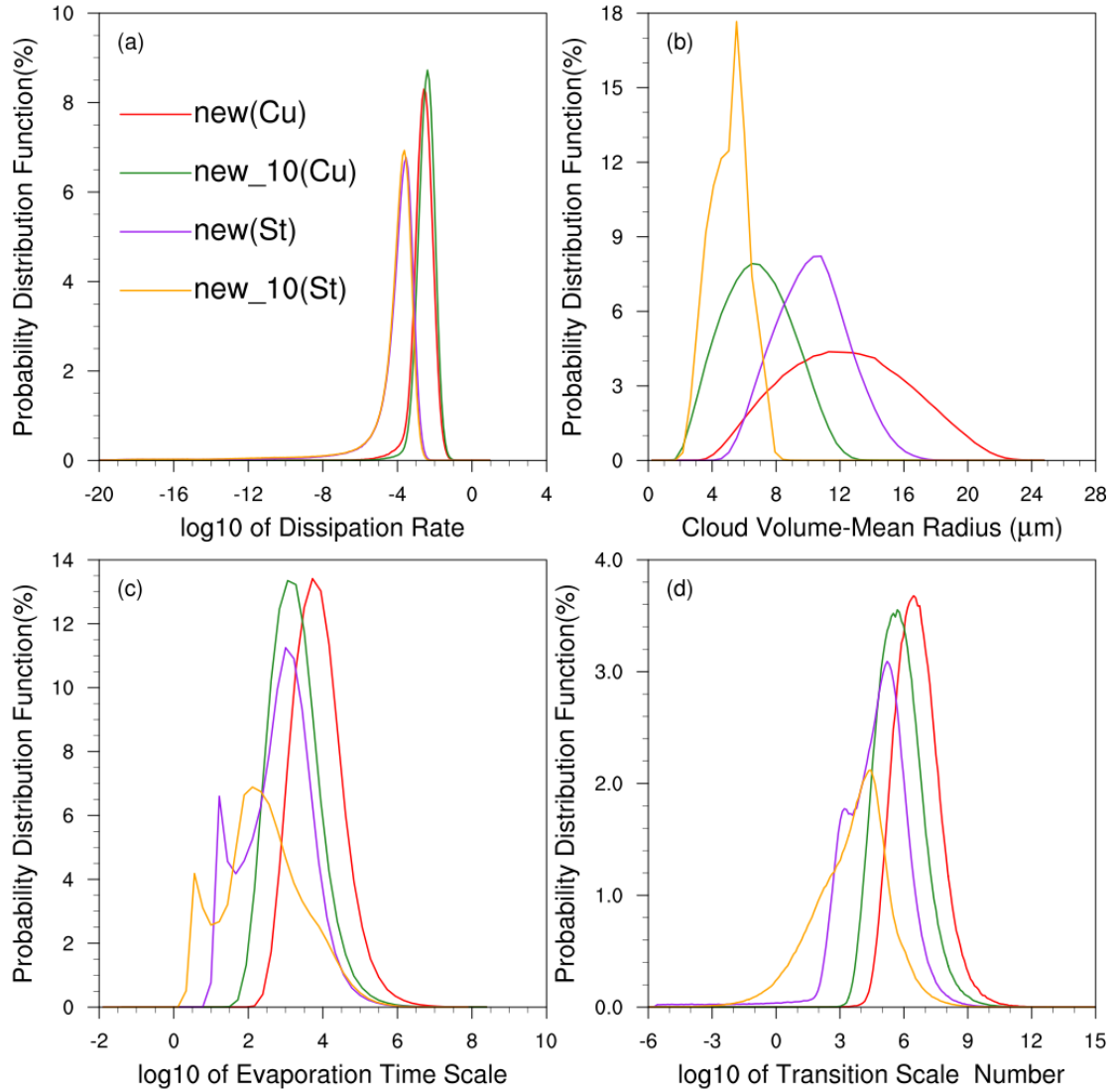
788

789 Figure 4. Time series of (a) domain-averaged cloud fraction and (b) total downward
 790 irradiance at the central point from the observation and the *default* experiment in the
 791 stratocumulus case.



792

793 Figure 5. The temporal evolutions of main cloud microphysical and optical properties
 794 in all simulation experiments for the stratocumulus case, including (a) cloud water
 795 mixing ratio (q_c) (g/kg), (b) cloud droplet number concentration (N_c) (/cm³), (c) cloud
 796 droplet volume-mean radius (r_v) (μm), (d) cloud water path (CWP) (g/m²), and (e) cloud
 797 optical depth (τ). In (b), N_c in the experiments *default* and *new* are normalized by the
 798 maximum cloud droplet number concentration (N_{cmax}) from *default*, respectively; N_c in
 799 the experiments *default_10* and *new_10* are normalized by N_{cmax} from *default_10*,
 800 respectively. The four experiments are detailed in Table 1.



801

802 Figure 6. Probability distribution functions (PDFs) of (a) turbulence dissipation rate (ϵ),

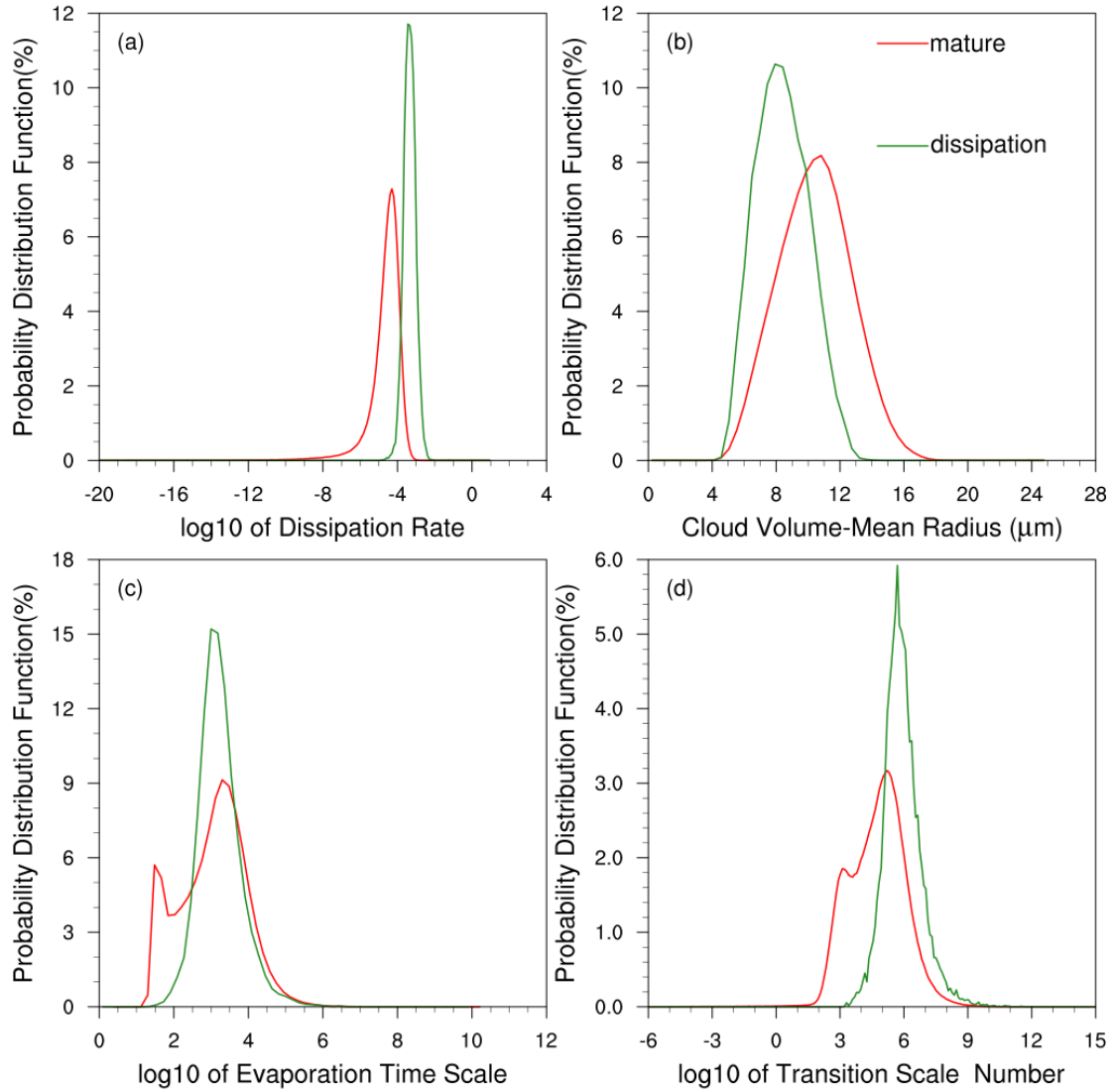
803 (b) cloud droplet volume-mean radius (r_v), (c) evaporation time scale (τ_{evap}), and (d)

804 transition scale number (N_L) of cloud grids experiencing the entrainment-mixing

805 process in the simulations with the new entrainment-mixing parameterization for the

806 cumulus case (Cu, the solid lines) and the stratocumulus case (St, the dash lines),

807 respectively. The experiments are detailed in Table 1.



808

809 Figure 7. Probability distribution functions (PDFs) of (a) turbulence dissipation rate (ϵ),

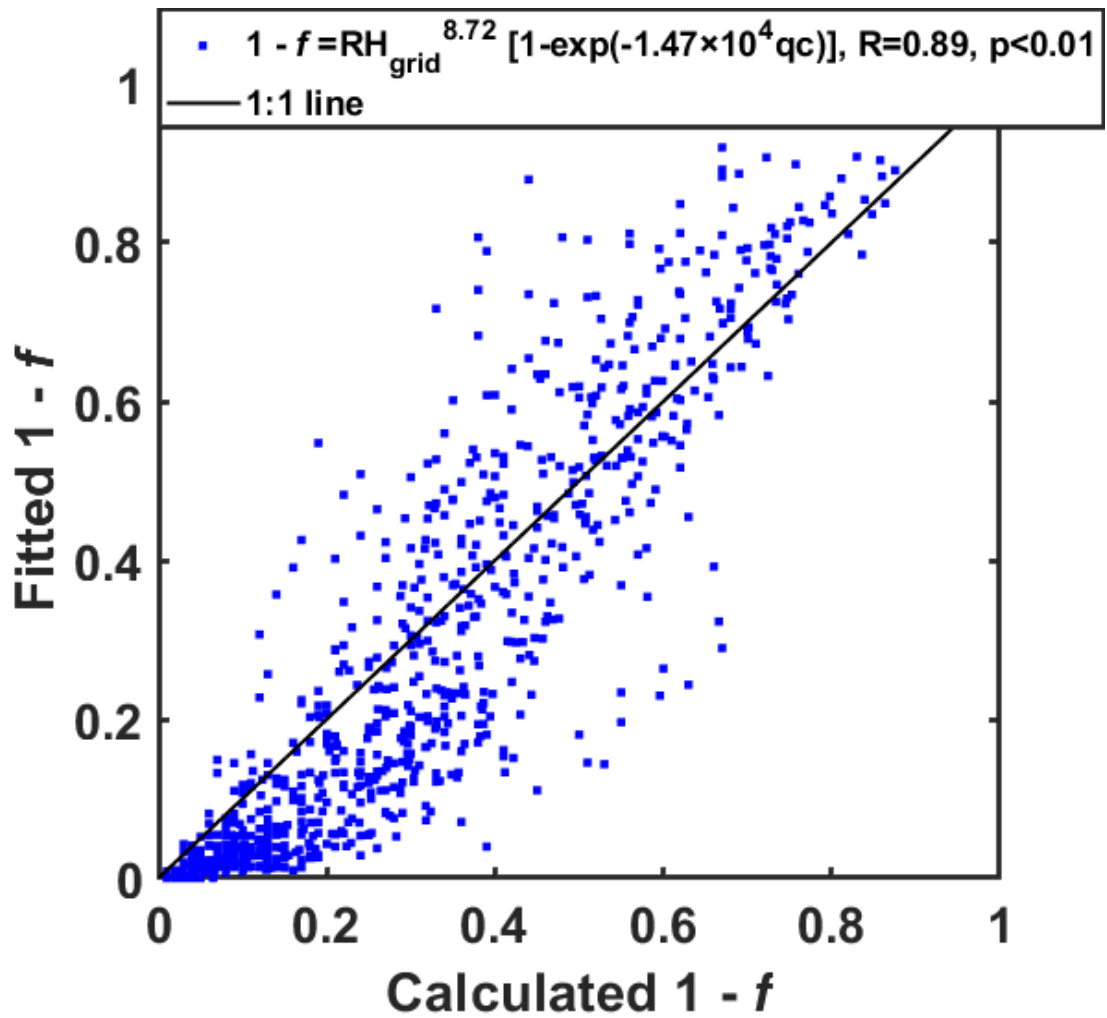
810 (b) cloud droplet volume-mean radius (r_v), (c) evaporation time scale (τ_{evap}), and (d)

811 transition scale number (N_L) of cloud grids experiencing the entrainment-mixing

812 process at the mature stage from 12:00 UTC to 16:00 UTC (the red lines) and the

813 dissipation stage from 21:00 UTC to 24:00 UTC (the green lines) in *new* for the

814 stratocumulus case. The experiment is detailed in Table 1.

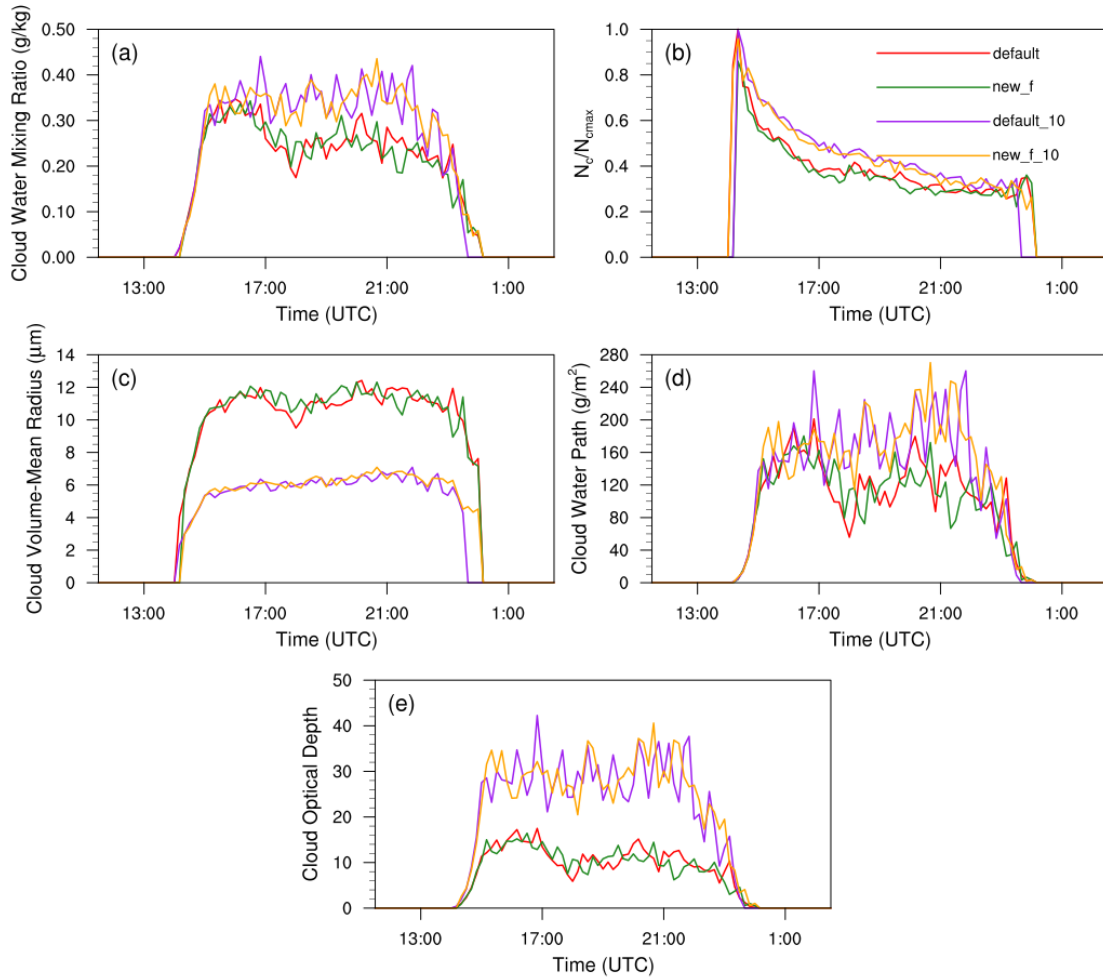


815

816 Figure 8. The fitted 1 - f as a function of the calculated 1 - f . The fitted 1 - f is obtained

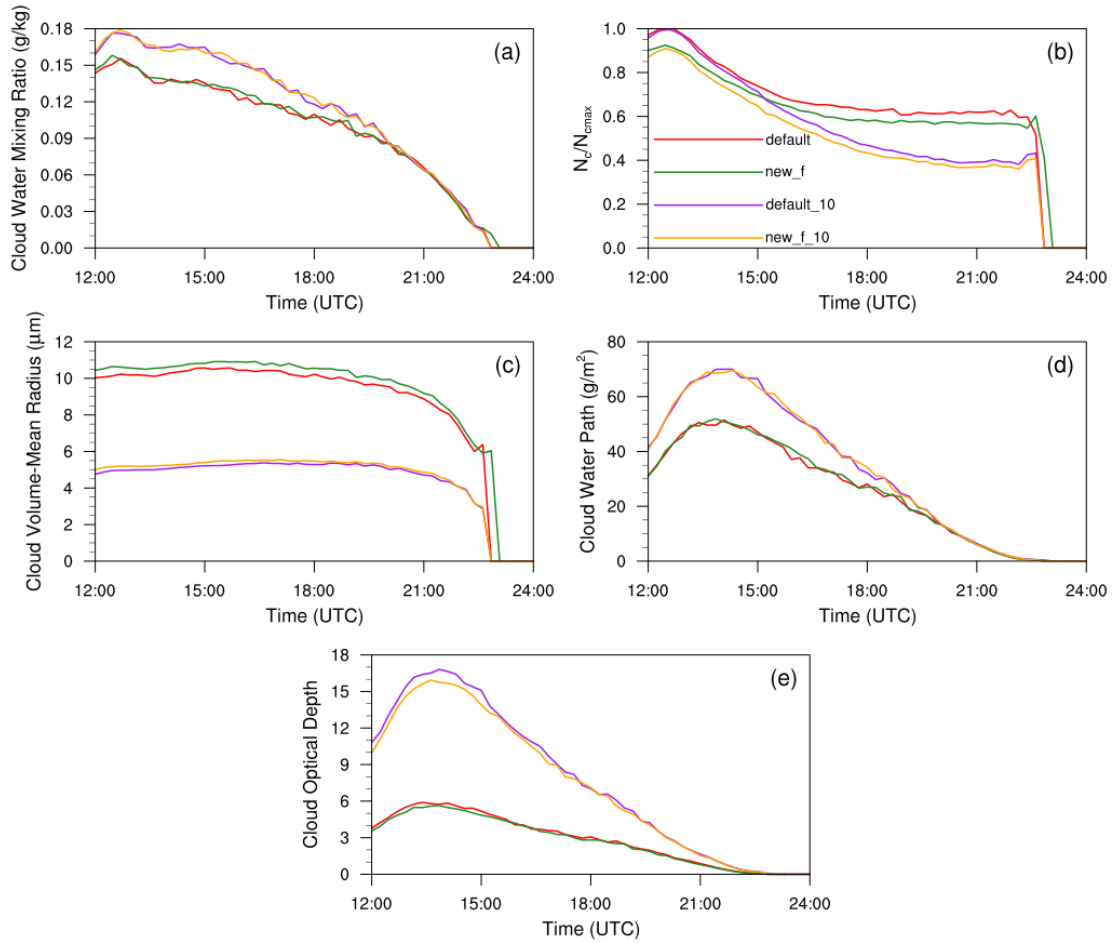
817 by the fitting functions with grid-mean relative humidity (RH_{grid}) and cloud water

818 mixing ratio (q_c). The black line denotes the 1:1 line.



819

820 Figure 9. The temporal evolutions of main cloud microphysical and optical properties
 821 in all simulation experiments for the cumulus case, including (a) cloud water mixing
 822 ratio (q_c) (g/kg), (b) cloud droplet number concentration (N_c) (/cm³), (c) cloud droplet
 823 volume-mean radius (r_v) (μm), (d) cloud water path (CWP) (g/m²), and (e) cloud optical
 824 depth (τ). In (b), N_c in the experiments *default* and *new_f* are normalized by the
 825 maximum cloud droplet concentration (N_{cmax}) from *default*, respectively; N_c in the
 826 experiments *default_10* and *new_f_10* are normalized by N_{cmax} from *default_10*,
 827 respectively. *new_f* and *new_f_10* are the experiments using entrained air relative
 828 humidity.



829

830 Figure 10. The temporal evolutions of main cloud microphysical and optical properties

831 in all simulation experiments for the stratocumulus case, including (a) cloud water

832 mixing ratio (q_c) (g/kg), (b) cloud droplet number concentration (N_c) (/cm³), (c) cloud

833 droplet volume-mean radius (r_v) (μm), (d) cloud water path (CWP) (g/m²), and (e) cloud

834 optical depth (τ). In (b), N_c in the experiments *default* and *new* are normalized by the

835 maximum cloud droplet number concentration ($N_{c,max}$) from *default*, respectively; N_c in

836 the experiments *default_10* and *new_10* are normalized by $N_{c,max}$ from *default_10*,

837 respectively. *new_f* and *new_f_10* are the experiments using entrained air relative

838 humidity.

839